

**Tuning CO₂ hydrogenation selectivity on Ni/TiO₂ catalysts
via sulfur addition**

Journal:	<i>Catalysis Science & Technology</i>
Manuscript ID	CY-ART-07-2022-001280.R2
Article Type:	Paper
Date Submitted by the Author:	28-Sep-2022
Complete List of Authors:	Le Berre, Carole; INPT, LCC-Composante ENSIACET Falqui, Andrea; University Milano Casu, Alberto; King Abdullah University of Science and Technology Debela, Tekalign Terfa; University of Oregon, Chemistry and Biochemistry Barreau, Mathias; ICPEES Hendon, Christopher; University of Oregon, Chemistry and Biochemistry Serp, Philippe; INPT, LCC-Composante ENSIACET

ARTICLE

Tuning CO₂ hydrogenation selectivity on Ni/TiO₂ catalysts via sulfur addition

Received 00th January 20xx,
Accepted 00th January 20xx

Carole Le Berre,^a Andrea Falqui,^b Alberto Casu,^c Tekalign T. Debela,^d Mathias Barreau,^e Christopher H. Hendon,^d Philippe Serp^{a,*}

DOI: 10.1039/x0xx00000x

In the context of CO₂ valorization, the possibility of shifting the selectivity of Ni catalysts from CO₂ methanation to reverse water gas shift reaction could be economically attractive provided the catalyst presents sufficient activity and stability. Remarkably, the addition of sulfur (0.2-0.8% w/w) to nickel on a Ni/TiO₂ catalyst induces a complete shift in the catalyst selectivity for the CO₂ hydrogenation at 340 °C from 99.7% CH₄ to 99.7% CO. At an optimal Ni/S atomic ratio of 4.5, the productivity of the catalyst reaches 40.5 mol_{CO₂}·mol_{Ni}⁻¹·h⁻¹ with a good stability. Density functional theory (DFT) calculations performed on various Ni surfaces reveal the key descriptor of selectivity is the binding energy of the CO intermediate, which is related to the local electron density of surface Ni sites.

Introduction

Efficient CO₂ conversion using green H₂ coming from renewable sources represents a potential way to limit global CO₂ emission. Useful CO₂-derived C1 building blocks, such as formic acid, carbon monoxide, methanol and methane can be obtained from the catalytic hydrogenation of CO₂. Among these C1 building blocks, CO, which can be used as syngas component to be subsequently transformed into liquid fuels via Fischer-Tropsch synthesis (FTS), and CH₄, which represent a pillar of the power-to-gas technology,¹ are particularly attractive. On supported nickel catalysts the reaction leads to methane formation (Sabatier reaction).^{2, 3} Noble metal-based catalysts are usually preferred for CO production *via* the reverse water gas shift reaction (RWGSR).⁴ Considering the low cost of nickel compared to noble metals, shifting the selectivity of Ni catalysts from methanation to RWGSR could be economically attractive provided the catalyst present sufficient activity and stability.

It was recently reported that supported Ni single atoms⁵⁻⁷ and to a lesser extent supported Ni clusters⁸⁻¹² could be active for the RWGSR, unravelling structure sensitivity in Ni-catalyzed CO₂ hydrogenation (decreasing CO adsorption strength with

decreasing particle size). However, such catalysts present the drawback of being difficult to prepare at high metal loadings and on a large scale for industrial use. Another way to shift the selectivity of Ni towards CO is to modify its valence state such as in perovskites,^{13, 14} since the CO binding energy is much weaker on oxidized- than on metallic-Ni.¹⁵ At 400 °C, a LaFe_{0.5}Ni_{0.5}O₃ catalyst allows a STY of 8.7 mol_{CO}·mol_{Ni}⁻¹·h⁻¹ with S_{CO} of 96.6 %.¹³

Tuning selectivity of Ni catalysts was also achieved by controlling the nature of the metal-oxide interfacial sites,¹⁶ which are suspected to be key species for the methanation of CO₂ and the RWGSR reaction.¹⁷⁻²¹ Experimental and theoretical results have demonstrated that on Ni₃Fe₃/ZrO₂ catalysts, the interaction of the Ni-ZrO₂ interface with CO was strong enough to facilitate CH₄ formation, while weak CO interaction on the Ni-FeO_x interface of Ni₃Fe₃/ZrO₂ catalysts made it desorb as the reaction product (at 400 °C, STY = 82.5 mol_{CO}·mol_{Ni}⁻¹·h⁻¹ - S_{CO} = 95.8 %).¹⁶ Modifications in the Ni electronic structure can also be achieved by pretreating conventional Ni supported catalysts. For example, it has been demonstrated that the selectivity of Ni/SiO₂ catalysts was found to change from CH₄ to CO after a CO₂ hydrogenation cycle from 100 to 800 °C, due to the formation of Ni₃C presenting a lower CO adsorption energy than metallic Ni.²² The formation of alloys²³ or intermetallic compounds²⁴ is also an efficient way to tune the metal d-band center, which proves to be instructive in assessing the binding energy of σ -donor intermediates, such as CO.

Sulfur has long been identified as a poison for Ni catalysts in CO-methanation, due to the quick and irreversible formation of inactive NiS sites that lead to the loss of catalytic activity due to geometric and electronic surface restructuring, terminally affecting the electronic properties of the Ni sites.²⁵⁻²⁹ The activity loss is particularly significant in the case of pre-

^a LCC-CNRS, INPT, 205 route de Narbonne, 31077 Toulouse Cedex 4, France.
E-mail : philippe.serp@ensiacet.fr

^b Department of Physics "Aldo Pontremoli", University of Milan, Via Celoria 16, 20133, Milan, Italy

^c King Abdullah University of Science and Technology (KAUST), Biological and Environmental Sciences and Engineering (BESE) Division, 23955-6900 Thuwal, Saudi Arabia

^d Department of Chemistry and Biochemistry, University of Oregon, Eugene, OR, USA

^e ICPEES-UMR 7515 CNRS-ECPM-Université de Strasbourg, 25 rue Becquerel, 67087 Strasbourg Cedex 2, France

Electronic Supplementary Information (ESI) available: catalytic performances, SEM, TEM, XRD, XPS, Raman, TPR and ESR analyses. See DOI: 10.1039/x0xx00000x

sulfided Ni catalysts.^{25, 29} For CO₂-methanation, on conventional supports such as alumina or silica, the presence of traces of sulfur impurities (H₂S, SO₂) in the feed gas,^{30,31} or the use of a sulfate precursor during catalyst preparation³² (the methanation being conducted without sulfur impurities), also result in drastic activity decrease. Thus, a Ni/SiO₂ catalyst prepared from Ni sulfate performed negligible activities for CO₂ hydrogenation because of the formation of inactive Ni₃S₂ during catalyst preparation.³² Interestingly, a higher tolerance of Ni catalysts to sulfur poisoning was evidenced when using a reducible support such as CeO₂, due to the thermodynamically favorable formation of the Ce₂O₂S phase that restricts the formation of nickel sulfide.³³ In addition, infrared studies on the effect of sulfur poisoning on the CO adsorption by Ni catalysts have shown that the strength of CO adsorption to surface nickel atoms was weaker on pre-sulfided catalysts.^{34, 35} Strong reduction or even blocking of CO adsorption upon sulfur addition to Ni(111) was also reported.³⁶ Finally, it is worth mentioning that (Fe,Ni)S clusters of natural enzymes, such as carbon monoxide dehydrogenase, efficiently and reversibly catalyze the reduction of CO₂ to CO.³⁷ Additionally, recent DFT calculation have shown the potentiality of sulfur-deficient FeS(001) surface for CO₂ activation and reduction.³⁸ In that latter case, a high sulfur vacancy density is expected to improve the catalytic activity of FeS-containing catalysts for the RWGSR. However, to the best of our knowledge, there are no discussions in the literature about controlling the selectivity of CO₂ hydrogenation by sulfur addition on Ni catalysts.

Herein we demonstrate the effect of sulfidation on the selectivity of the Sabatier reaction on Ni/TiO₂ catalysts. Using a combination of first-principles calculations and experiment we show that the selectivity of Ni_x/TiO₂ for the selective formation of CO over CH₄ can be tuned by controlling the extend of sulfidation (x). Our findings suggest that despite sulfur being a traditional poison for the Sabatier reaction on Ni, the extend of sulfidation offers one unique avenue to tune catalyst selectivity.

Results and discussion

Two Ni catalysts supported on the reducible oxide TiO₂ were first compared. The first one (10%Ni/TiO₂) was prepared by the incipient-wetness impregnation method from nickel nitrate using TiO₂-P25 as support (a mixture of TiO₂ rutile (80 %) and anatase (20 %) phases).¹⁸ The second one (10%Ni-S/TiO₂) was prepared similarly but the calcination was performed in the presence of SO₂, resulting after reduction in a sulfided catalyst. The catalytic performance using a flow reactor is shown in Fig. 1, and results obtained after the reaction reached a steady-state at 260 and 340 °C are summarized in Table 1.

It is noticed that at temperatures as low as 260 °C, the 10%Ni/TiO₂ catalyst produces selectively CH₄ ($S_{\text{CH}_4} = 98.7\%$) with a high activity ($56.5 \text{ mol}_{\text{CH}_4} \cdot \text{mol}_{\text{Ni}}^{-1} \cdot \text{h}^{-1}$), while CO is selectively produced on 10%Ni-S/TiO₂ ($S_{\text{CO}} = 98.3\%$) at a lower rate ($6.5 \text{ mol}_{\text{CO}} \cdot \text{mol}_{\text{Ni}}^{-1} \cdot \text{h}^{-1}$).

Table 1. CO₂ conversion, CH₄ and CO selectivity, and specific activity of Ni catalysts at 260 °C and 340 °C.

Catalyst	CO ₂ conv. (%) ^a	S _{CH₄} (%) ^a	S _{CO} (%) ^a	STY ^b
10Ni/TiO ₂	79.1 (99.7)	98.7 (99.7)	1.3 (0.3)	56.5 (72.1)
10Ni-S/TiO ₂	7.5 (29.2)	1.7 (0.3)	98.3 (99.7)	6.5 (25.2)

^a The values between parentheses are the value obtained at 340 °C. ^b In $\text{mol}_{\text{CH}_4} \cdot \text{mol}_{\text{Ni}}^{-1} \cdot \text{h}^{-1}$ for 10Ni/TiO₂ and in $\text{mol}_{\text{CO}} \cdot \text{mol}_{\text{Ni}}^{-1} \cdot \text{h}^{-1}$ for 10Ni-S/TiO₂. Reaction conditions: 200 mg catalyst, $F/W = 16\,500 \text{ mL} \cdot \text{g}^{-1} \cdot \text{h}^{-1}$, $\text{H}_2/\text{CO}_2 = 4$, $P = 6.1 \text{ bar}$.

As CH₄ selectivity can increase at high CO₂ conversion, we also run the 10%Ni/TiO₂ catalyst at lower conversion (Fig. S1). Under these conditions (higher F/W ratio), the CO₂ conversion at 260 °C (4.3%) is similar to that obtained with Ni-S/TiO₂ (7.5 %), and the Ni/TiO₂ catalyst is still very selective for CH₄ ($S_{\text{CH}_4} > 94\%$). The temperature increase (up to 400 °C) significantly affects the CO₂ conversion, but not the selectivity (Fig. S2). This sulfided catalyst shows interesting performances compared to other nickel catalysts active for the RWGSR reported in the literature (Table S1). Indeed, a selectivity of 99.1% and a CO₂ conversion rate of $60.6 \text{ mol}_{\text{CO}_2} \cdot \text{mol}_{\text{Ni}}^{-1} \cdot \text{h}^{-1}$ were obtained, which are similar to those obtained on a Ni/SiO₂ catalyst presenting a nickel carbide-like phase obtained after surface modification upon exposure to CO₂/H₂ or CH₄ atmospheres under high temperature.²² The F/W ratio was further increase to $33\,000 \text{ mL} \cdot \text{g}^{-1} \cdot \text{h}^{-1}$ without impact on the selectivity (Fig. S3, Table S1). As expected,³⁹ the CO₂ conversion decreased with the increase in F/W because of the shorter contact time and the decrease in the adsorbed reactant content on the catalyst surface.

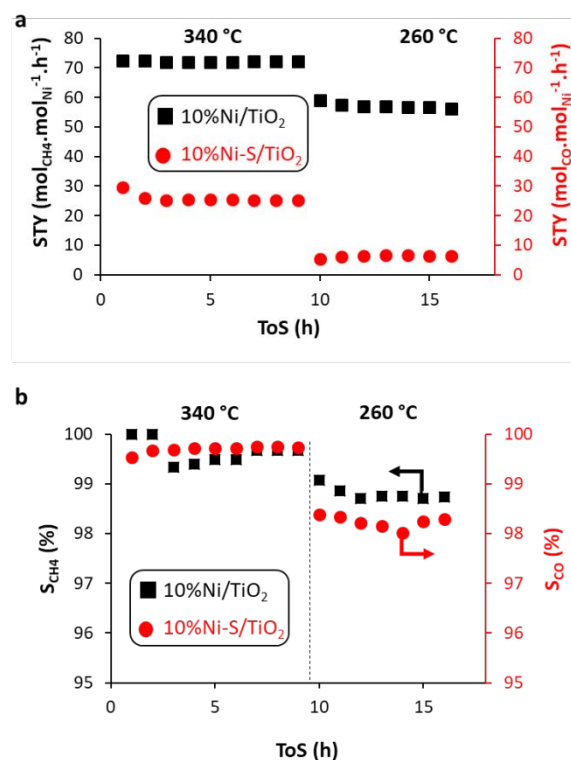


Figure 1. Comparison of: a) STY in CO₂ methanation; and b) CH₄/CO selectivity for 10Ni/TiO₂ (black squares) and 10Ni-S/TiO₂ (red circles) catalysts at 340 and 260 °C. Reaction conditions: 200 mg catalyst, $F/W = 16\,500 \text{ mL} \cdot \text{g}^{-1} \cdot \text{h}^{-1}$, $\text{H}_2/\text{CO}_2 = 4$, $P = 6.1 \text{ bar}$.

It was checked that the operative pressure has no influence on the selectivity of the reaction (see Fig. S4 for the performance obtained at atmospheric pressure). A 1%Pt/TiO₂ catalyst (effective loading from ICP 1.02%) was also prepared for comparison purpose, since Pt based catalyst are conventional RWGS catalysts.⁴⁰ The comparison of the catalytic performance (Fig. S5) shows that the 10%Ni-S/TiO₂ catalyst compared favorably at 340 °C, which is an excellent result considering the price of Pt metal. We nevertheless note that at 400 °C (Fig. S2), the catalyst tends to slightly deactivate upon time on stream, and starts to form more CH₄, likely due to a partial reduction of some sulfide species, as discussed later.

ICP analyses show Ni contents of 9.1 and 7.6% w/w for 10%Ni/TiO₂ and 10%Ni-S/TiO₂ catalysts, respectively. Elemental analysis show a S contents of 0.32% w/w for the 10%Ni-S/TiO₂ catalyst (Table 2); this correspond to an atomic % of sulfur of 7.1% related to Ni. SEM observations performed on both catalysts (Fig. S6) do not show remarkable morphological differences. Fig. 2 shows STEM and STEM-HAADF images of the two freshly reduced catalysts. Particle size distributions based on total particle number and on total atom number⁴¹ are shown on Fig. S7. The average particle size for the 10%Ni/TiO₂ and 10%Ni-S/TiO₂ catalysts are 13.3 and 7.6 nm, respectively (Table 2). The smaller mean particle size obtained on the Ni-S/TiO₂ catalyst could be the result of a different metal-support interaction and an easier reduction for this catalyst, as discussed later. EDX analyses (Fig. S8) were performed on the reduced catalysts to check for the presence of sulfur. Sulfur was not detectable on the 10Ni/TiO₂ catalyst, neither on the support nor on the Ni. For the 10Ni-S/TiO₂ catalyst, sulfur was detected on the Ni particles (at. % of S related to Ni between 2 and 15%), but was not detectable on the support.

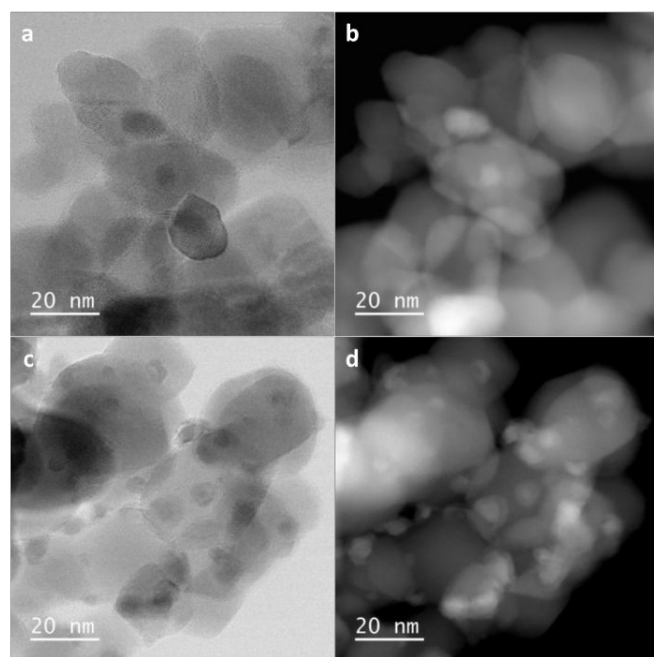


Figure 2. STEM and STEM-HAADF micrographs for the reduced: **a,b** 10%Ni/TiO₂; and **c,d** 10%Ni-S/TiO₂ catalysts.

Thus, if TiO₂-SO₄⁻ species could be formed upon catalyst calcination under SO₂/air mixtures,⁴² these species should disappear upon catalyst reduction. To verify this hypothesis, we independently study by XRD the reaction of TiOSO₄·xH₂O reference compound under the conditions used for catalyst reduction. The data obtained (Fig. S9) point to the complete transformation of TiOSO₄·xH₂O into anatase TiO₂ under these reducing conditions.

HRSTEM-HAADF analysis of the 10%Ni-S/TiO₂ catalyst provided better-defined information from a spatial point of view and highlighted the seldom presence of small-sized nanoparticles at the edges of wider crystalline domains. While the structures of the latter are compatible with TiO₂, local Fourier analysis performed on these small nanoparticles (< 5 nm) that showed a sufficiently clear structural projection, resulted in finding different sets of interplanar distances and angular relationships that could be ascribed to distinct phases of nickel sulfide, namely to NiS, NiS₂ and Ni₃S₂ (Fig. 3). To understand the structural transformation of the catalyst during the sulfidation, XRD analyses were performed (Fig. S10). The Ni diffraction peaks of the 10Ni/TiO₂ catalyst (2θ = 44.5°, 51.9°, and 76.3°) correspond to the (111), (200), and (220) crystal faces of Ni. For the 10Ni-S/TiO₂ catalyst, these peaks are much wider and less intense, but still present (2θ = 44.3°, 51.9°, and 76.3°). Given the low occurrence and the small size of many of the crystalline nickel sulfide nanoparticles observed by HRSTEM-HAADF analysis, the presence of a crystalline sulfided phase (NiS, NiS₂ or Ni₂S₃) could not be clearly detected by XRD, but the wide peaks observed could also fit some peaks of Ni sulfide phases. Finally, the presence of amorphous nickel sulfide nanoparticles cannot be ruled out from STEM and XRD analyses.

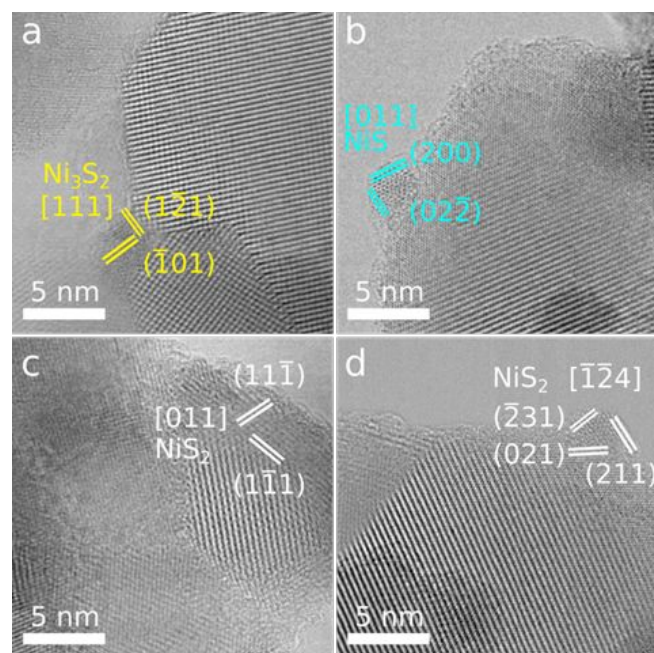


Figure 3. Representative HRSTEM-HAADF micrographs for the 10%Ni-S/TiO₂ catalyst, showing small crystal domains of different nickel sulfide phases with interplanar distances indicated in false colors: **a** Ni₃S₂ (yellow), **b** NiS (cyan), **c,d** NiS₂ (white).

Table 2. Catalyst characterization.

Catalyst	Ni (%)	S (%)	BET surface area (m ² /g)	Ni particle size (nm) ^a	Ni particle size (nm) ^b
10%Ni/TiO ₂	9.1	0	42.9	16.5	13.3 ± 1.8
10%Ni-S/TiO ₂	8.3	0.32	49.1	9.2	7.6 ± 1.5

^a From XRD. ^b From TEM.

The Ni crystallite size measured by XRD was 16.5 and 9.2 nm for the 10%Ni/TiO₂ and 10%Ni-S/TiO₂ catalysts, respectively; which is in good accordance with the STEM-HAADF measurements. XPS analyses were performed just after reducing the samples at 400 °C. Fig. S11 presents the high-resolution Ni 2*p*, S 2*p* and Ti 2*p* spectra of the two samples. The Ni 2*p* spectra are composed of two spin-orbit doublets (2*p*_{1/2} and 2*p*_{3/2}) and shakeup satellites. For the 10%Ni/TiO₂ catalyst (Fig. 4a), Ni is present as Ni⁰ (main peak at 852.6 eV),⁴³ NiO (multiplet-split peaks at 853.7 and 855.8 eV)⁴⁴ and possibly Ni(OH)₂ (855.8 eV).^{45, 46} The presence of significant amount of Ni⁰ can explain the high selectivity for methane obtained with this catalyst. The Ni 2*p*_{3/2} core-level spectrum of the 10%Ni-S/TiO₂ catalyst is significantly different (Fig. 4b), showing a very small contribution of Ni⁰ (852.6 eV) and an intense peak at 856.3 eV, which could arise from Ni(OH)₂, NiS (855.7 eV),⁴⁷ Ni₃S₂ (855.7-856.1 eV)^{48, 49} and/or NiS₂ (855.7-855.9 eV).^{50, 51} The Ni/S surface atomic ratios of 10%Ni-S/TiO₂ catalyst allows calculating an atomic % of S related to Ni of 7.6% (in good accordance with the values obtained from elemental and EDX analyses) that precludes the exclusive formation of NiS. For the S 2*p* spectrum, the peak at 162.1 eV corresponds to divalent ions (S²⁻) involved in metal-sulfur bonds,⁵² which could correspond to NiS (161.6 eV), Ni₃S₂ (162.2 eV) and/or NiS₂ (162.4 eV).^{51, 53} The peak at 168.9 eV is associated with sulfate species resulting from surface oxidation of NiS_x species.^{51, 54} The high-resolution Ti 2*p*_{3/2} XPS spectra of the 10%Ni/TiO₂ and 10%Ni-S/TiO₂ catalysts are shown in Fig. 4c. For 10%Ni/TiO₂, the Ti 2*p*_{3/2} and Ti 2*p*_{1/2} peaks centered at binding energies of 459.3 and 465.2 eV (Fig. S10) are typical of the Ti⁴⁺-O bonds in TiO₂. In 10%Ni-S/TiO₂, the envelop of the Ti 2*p*_{3/2} peak is broader due to the presence of Ti³⁺ species at 458.3 eV, resulting from the creation of surface oxygen vacancies (O_v).⁴⁷ The attribution of the 458.3 eV component to titanium(IV) oxysulfate species must be excluded on the basis of XPS measurements over TiOSO₄·xH₂O reference compound (Fig. S12). The formation of O_v upon sulfidation/reduction was confirmed by Raman analyses (Fig. S13). The lowest frequency vibrational mode E_g(1) at 140 cm⁻¹ characteristic of TiO₂ in 10%Ni/TiO₂ shows pronounced broadening and blue-shift (149 cm⁻¹) in 10%Ni-S/TiO₂. Theoretical calculations proposed that the broadening and blue-shift resulted from the presence of localized lattice defects associated with surface O_v.⁵⁵ The formation of O_v on TiO₂ leads to the creation of unpaired electrons or cationic Ti³⁺ centers observable by EPR.^{56, 57}

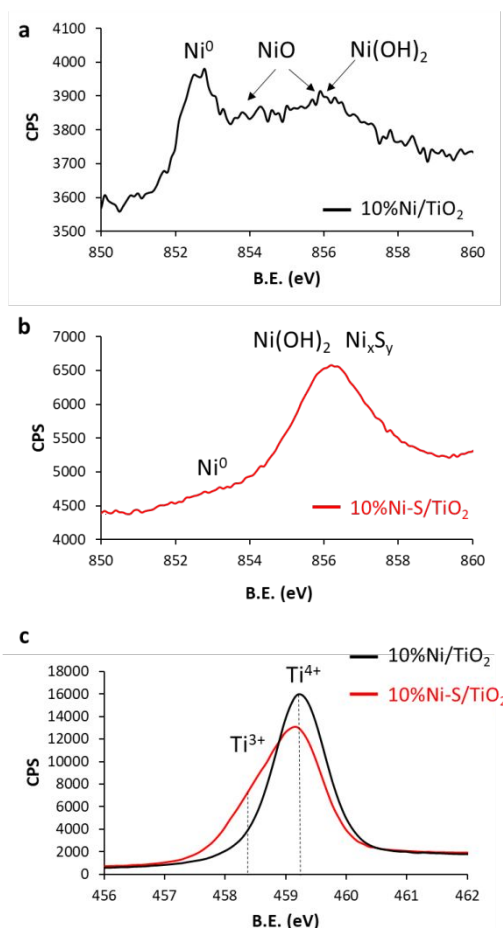


Figure 4. Ni 2*p* XPS spectra of 10%Ni/TiO₂ a and 10%Ni-S/TiO₂ b; and c Ti 2*p* XPS spectrum of Ni-S/TiO₂ and Ni/TiO₂.

The EPR spectrum of 10%Ni-S/TiO₂ (Fig. S14) shows a broad EPR resonance line at *g* = 2.156, which could arise from surface exposed Ti³⁺ sites but also to Ni³⁺ species.^{58, 59} The presence of significant amount of O_v on the 10%Ni-S/TiO₂ catalyst can be of importance for the CO₂ hydrogenation reaction. Indeed, it has been proposed that on Ni/TiO₂ catalysts, the presence of Ti³⁺ species, which likely altered the SMSI between Ni and the support, allows the enhancement of CO₂ hydrogenation activity.⁶⁰ It is also known that Ni^{δ-}-O_v-Ti³⁺ interfacial sites on Ni/TiO₂ catalysts serve as dual-active site to efficiently catalyse the WGSR.⁶¹⁻⁶³

The TPR profiles of the supported nickel catalysts are shown in Fig. S15. They indicate a different metal-support interaction in the two catalysts. The reduction temperature maxima (RTM) peaks were located at 510 °C for 10%Ni/TiO₂ and 460 °C for 10%Ni-S/TiO₂. Similar differences in RTM have been reported for Ni/Al₂O₃ and NiSO₄/Al₂O₃ catalysts.⁶⁴ Also, the shape of the TPR curve for the 10%Ni-S/TiO₂ catalysts is less symmetrical, which indicates a less uniform state of the nickel species in this catalyst. The reduction peak of the 10% Ni-S/TiO₂ catalyst begins at 360 °C, which may explain the slight catalyst deactivation observed when the RWGS is carried out at 400 °C (Fig. S2).

Together, the 10%Ni/TiO₂ catalyst presents several features of a good methanation catalyst: relatively large particle size and predominance of Ni⁽⁰⁾.¹⁸ The 10%Ni-S/TiO₂ catalyst contains significant amounts of O_v on the support, which are active for CO₂ activation.¹² This catalyst contains few Ni⁽⁰⁾ for H₂ activation (H₂ heterolytic dissociation can also occur on sulfided catalysts⁶⁵), and significant amounts of amorphous and crystalline NiS_x species. As it has been shown that the strength of CO adsorption to surface Ni atoms was weaker for pre-sulfided catalysts,^{34, 35} we can propose that this is the origin of the high selectivity for RWGSR observed for the Ni-S/TiO₂ catalyst.

In order to understand the correlation between the binding energy of CO with the product selectivity, we calculated the CO adsorption energies (E_a) for Ni(111), Ni₃S₂(001), NiS(100) and NiS₂(111) surfaces using the spin-polarized DFT. We sampled several plausible CO binding modes to various facets of the Ni_xS_y systems (Fig. S16 and Table S2), and show the most stable CO-bound configurations in Fig. 5. We find the binding energies to be -1.57, -1.47, -0.73, and -1.20 eV for Ni(111), Ni₃S₂(001), NiS(100), and NiS₂(111) surfaces, respectively. The results indicate that the Ni(111) surface binds CO most strongly. The addition of sulfur leads to weakening of the CO binding. The CO binding energy is inversely proportional to the degree of sulfidation. We can understand this through examination of the Ni d-band center. Since CO is both a σ -donor and π -acceptor, the CO bond energy should be reduced as the metal d-states are occupied, as the d-center is a descriptor for σ -accepting ability. Thus, a downward shift of the d-band center is considered favorable because it correlates with the decrease in adsorption energies of typical catalytic σ -donor and π -acceptor poisons, such as CO, resulting in the turnover of surface active sites.⁶⁶

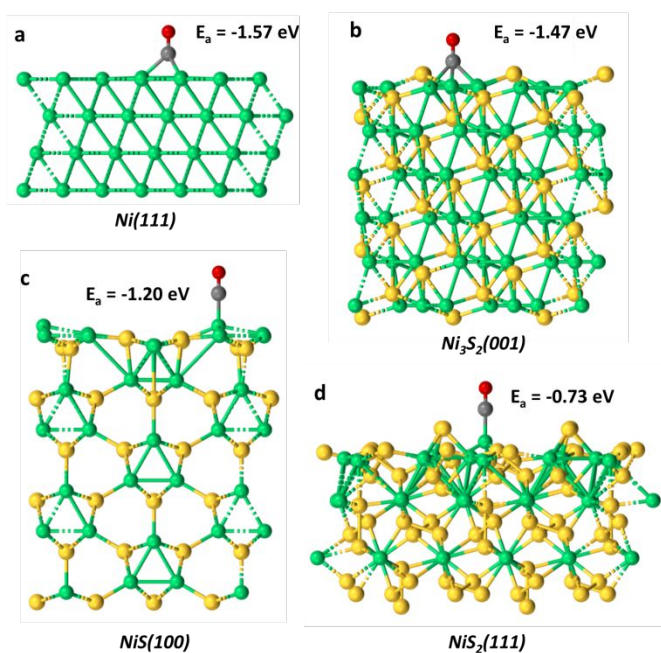


Figure 5. DFT equilibrated structure of CO chemisorbed on a) Ni(111), b) Ni₃S₂(001), c) NiS(100), and d) NiS₂(111) and surfaces.

In our case, the calculated Ni d-band centers are -0.30, -1.14, -1.34, and -1.37 eV for Ni(111), Ni₃S₂(001), NiS(100), and NiS₂(111) surfaces, respectively. This trend supports the hypothesis that sulfidation is one route to affecting CO-binding energies, thereby affecting the catalytic preference to form CO over CH₄. We also considered possible CO₂ binding sites on the Ni_xS_y systems (Fig. S17), but did not include the energetics of these species in this study. Instead, we focus on the CO binding energy as an energetic descriptor for selectivity.

Finally, as the Ni/S atomic ratio could have an influence on both activity and selectivity, we used different pre-sulfided catalysts showing sulfur atomic percentage related to nickel between 4.5 and 15% (based on elemental and ICP analyses) to evaluate its impact. Figure 6 shows the catalytic performances of these catalysts for the RWGSR performed at 340 °C. In the investigated range, the atomic % of sulfur related to Ni significantly affects catalyst activity, with an optimum value at 4.5%, but has no influence on selectivity.

Conclusions

In summary, we have demonstrated a facile strategy to tune the selectivity of Ni/TiO₂ catalyst in the CO₂ hydrogenation reaction. Calcination of the Ni/TiO₂ catalyst under SO₂-air mixtures allows after reduction to obtain a sulfided Ni-S/TiO₂ catalyst. The sulfided catalyst contains significant amounts of O_v to activate CO₂, metallic nickel or sulfided Ni⁶⁷ for H₂ activation and significant amounts of amorphous and crystalline NiS_x species. Compared to the Ni/TiO₂ catalyst that produces selectively CH₄ in the 260-400 °C temperature range, the Ni-S/TiO₂ catalyst is less active but selectively produces CO in the same temperature range, while maintaining a good stability below 340 °C. According to DFT calculations, the key descriptor of selectivity is the CO binding energy to the Ni surface, which is related to the position of the d-band centre of the Ni species. Notably, while sulfur has long been identified as a poison for Ni catalysts in CO-methanation, we have demonstrated that its association with Ni on a reducible support such as TiO₂ allows the production of a precious metal-free RWGSR catalyst.

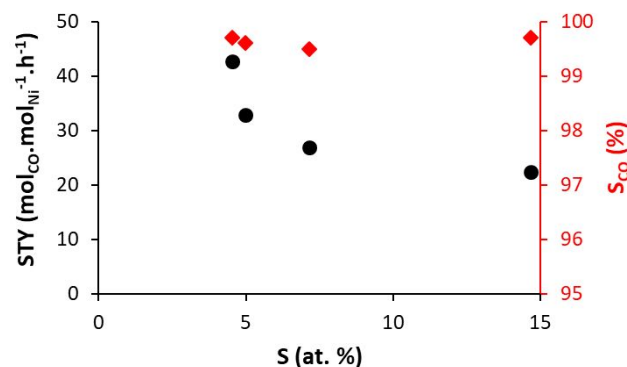


Figure 6. Comparison of: a) STY (black circles); and b) CO selectivity (red diamonds) for 10Ni-S/TiO₂ catalysts presenting various sulfur % related to Ni. Reaction conditions: T = 340 °C, 200 mg catalyst, F/W = 16 500 mL · g⁻¹ · h⁻¹, H₂/CO₂ = 4, P = 6.1 bar.

Experimental section

Catalyst preparation. The Ni catalysts were prepared by using an impregnation method. Ni(NO₃)₂ · 6H₂O (99.9% Strem Chemical) was dissolved in water, where TiO_{2-P25} (99.5%, Aeroxide, Aldrich) was then added. The desired quantity of Ni(NO₃)₂ · 6H₂O to reach a 10% w/w was used. The mixture was stirred during 4 h. The water was evaporated to obtain the catalyst, which was dried at 120 °C overnight, and calcined at 500 °C during 6 h under air to produce the calcined 10%Ni/TiO₂ catalyst. A similar procedure was followed to prepare the 10%Ni-S/TiO₂ catalyst, but in that case the calcination was performed in the presence SO₂-air mixtures obtained by mixing SO₂ with air, with the SO₂ concentration in the gas-air mixture being in the range of 0.2-5 g/m³. The amount of nickel deposited on each support was determined by Inductively Coupled Plasma (ICP) analyses.

A 1% Pt/TiO₂ catalyst was also prepared for comparative purpose by using the impregnation method from tetraammineplatinum(II) nitrate.

Catalyst characterization. The structural and textural properties of the catalysts were evaluated using different characterization techniques. The Brunauer-Emmett-Teller (BET) surface area, pore volume and pore size distribution of the samples were measured using a Quantachrome autosorb instrument with N₂ automatic injection. This method permits to obtain the N₂ adsorption/desorption isotherms at -196 °C. All the samples were pretreated under vacuum at 90 °C for 1 h to remove adsorbed water, then at 250 °C during 10 h for all other physisorbed species.

For the Temperature-Programmed Reduction (TPR) experiment (Micromeritics AutoChem 2920 Analyzer), the catalyst (100 mg) was introduced in a U-shaped tube and placed in an oven. Firstly, it was heated to 200 °C (10 °C·min⁻¹) for 1 h. After the reactor cooled to room temperature, an argon flow (30 mL·min⁻¹) swept the sample for 30 minutes. In a second step, the catalyst was reduced under a gaseous mixture of 10% H₂/Ar (30 mL·min⁻¹) with a heating ramp of 10 °C·min⁻¹ to 850 °C. The amount of hydrogen consumed was monitored using a TCD. Peaks of hydrogen consumption were obtained as a function of the temperature.

The distribution, shape and size of the metal particles were obtained using a JEOL JEM 1011 transmission electron microscope (TEM). The high-resolution analyses were conducted by using a JEOL JEM 2100F equipped with a field emission gun (FEG) operating at 200 kV with a point resolution of 2.3 Å and a JEOL JEM-ARM200F Cold FEG operating at 200 kV with a point resolution of > 1.9 Å.

The crystalline structure of the samples was determined by a D8 Advance Bruker Diffractometer (XRD). The surface of a sample to a depth of 1 to 10 nm was observed by X-ray Photoelectron Spectroscopy (XPS) using a Thermo Scientific K-alpha spectrometer equipped with an aluminum monochromatic source (Al Kα, hν = 1486.6 eV). Raman measurements were recorded with a Raman Horiba Jobin Yvon Labram HR 800 spectrometer in backscattering geometry using an optical objective 100 (NA 0.9). The wavelength of the

incident laser was 532 nm and its power was set to 1 mW. EPR data were recorded using an Elexsys E 500 Bruker spectrometer, operating at a microwave frequency of ≈9.5 GHz. All spectra were recorded using a microwave power of 10 mW across a sweep width of 1500 G (centred at 3100 G) with a modulation amplitude of 2 G. Experiments were carried out at 10 K using a liquid helium cryostat.

Catalytic tests. The catalytic tests of CO₂ hydrogenation were performed using a continuous-flow stainless steel fixed bed reactor (height = 300 mm, e.d. = 9.52 mm, i.d. = 7.9 mm) under a total pressure of 6.1 bar. 200 mg of catalyst with a particle size in the 100-200 μm range were mixed with 1800 mg of SiC (Alfa Aesar). Before the catalytic test, the catalyst was reduced in situ at 400 °C for 4 h under a 1/4 mixture of N₂/H₂, at atmospheric pressure. Then, experiments were performed at a constant F/W ratio (molar flow of reactant per mass of catalyst) of 16 500 mL (g·h)⁻¹. Catalytic tests were performed under a N₂/H₂/CO₂ gas mixture of 1/4/1 at 260, 300 and 340 °C and 6.1 bar. The composition of the reactant/product mixture was analyzed using an on-line gas chromatograph (500 Clarius) equipped with two TCD: one with argon as gas vector to quantify H₂, CH₄, and CO, and another with helium to quantify CO₂. The GC is equipped with two Shincarbon columns (1/8, 2.0 mm, 80/100), and recorded the formation of methane and conversion of H₂ and CO₂ every 8 min.

The different response coefficients determined from the GC calibration allowed us to calculate the molar fractions (X) of the different molecules considered during the methanation reaction, as follows:

$$X_A = \left(\frac{\text{Area of A signal}}{\text{Area of N}_2 \text{ signal}} \times N_2 \text{ flow} \right) \times \frac{1}{k_A}$$

With a = CO₂, CH₄, H₂, CO and k = response coefficient. The conversion rates of the reagents were then calculated as follows:

$$\text{CO}_2 \text{ conversion (\%)} = \left(1 - \frac{X_{\text{CO}_2}}{X_{\text{CO}_2} + X_{\text{CH}_4} + X_{\text{CO}}} \right) \times 100\%$$

$$\text{H}_2 \text{ conversion (\%)} = \left(1 - \frac{\text{H}_2 \text{ Output flow}}{\text{H}_2 \text{ Input flow}} \right) \times 100\%$$

With H₂ output flow = dry flow output × X_{H₂}.

$$\text{Dry flow output} = \left(\frac{\text{CO}_2 \text{ input flow}}{X_{\text{CO}_2} + X_{\text{CH}_4} + X_{\text{CO}}} \right)$$

$$\text{CH}_4 \text{ yield (\%)} = \left(\frac{\text{CH}_4 \text{ output flow}}{\text{CO}_2 \text{ input flow}} \right) \times 100\%$$

CH₄ output flow = dry flow output × X_{CH₄}.

CO Yield (%) = % CO₂ conversion – CH₄ Yield (%)

$$\text{CH}_4 \text{ selectivity (\%)} = \left(\frac{\text{CH}_4 \text{ yield (\%)}}{\% \text{CO}_2 \text{ conversion}} \right) \times 100\%$$

$$CO \text{ selectivity (\%)} = \left(\frac{CO \text{ yield (\%)}}{\%CO_2 \text{ conversion}} \right) \times 100\%$$

We expressed the percentage of CO₂ consumed by unit of time and by mole of metal, which corresponds to the STY.

Computational details

First-principles calculations were performed using spin-polarized DFT as implemented in the Vienna *ab Initio* Simulation Package (VASP), version 5.4.4.^{68, 69} The projected augmented plane wave (PAW)^{70, 71} approach with a plane-wave kinetic energy cutoff of 500 eV, and the revised Perdew-Burke-Ernzerhof (RPBE)⁷² exchange-correlation functional were employed. The Methfessel-Paxton method with broadening of 0.1 eV is used for the slabs, while the Gaussian-smearing with 0.01 eV was used for CO molecule.

Ni(111), Ni₃S₂(001), NiS(100), and NiS₂(111) surfaces were used to model the slab geometry. A vacuum space of 20 Å was used along the *c*-direction (perpendicular to the slabs) to ensure no significant interaction between adjacent cells occurred. For each surface, several competing binding modes were examined, and the most stable was presented. The others are available in the Supporting Information. Structural optimization was performed until the average force was < 0.03 eV/Å and the total energy converged within 10⁻⁵ eV/atom. A Monkhorst-Pack *K*-point sampling of 3 × 3 × 1 was used for the slab geometry, while only Γ -point was used for the free CO molecule. The adsorption energy is defined as $E_a = E_{tot} - E_{pristine} - E_{mol}$, where E_{tot} , $E_{pristine}$, and E_{mol} are the calculated energy of the slab with adsorbate, the pristine slab, and the CO molecule in the gas phase, respectively.

The d-band center was computed by aligning the mean d-states from the density of states to the Fermi level, following the method presented elsewhere.⁶⁶

Author Contributions

Dr. Carole Le Berre: catalyst synthesis and characterization and catalytic experiments, data elaboration and interpretation, writing original draft; Dr. Andrea Falqui and Dr. Alberto Casu: electron microscopy studies, data elaboration and interpretation, Prof. Christopher H. Hendon and Dr. Tekalign Debela: modeling studies, data elaboration and interpretation; Dr. Mathias Barreau: XPS studies; Prof. Philippe Serp: conceptualization and supervision of all the activities. All the authors contributed to the result discussion and review & editing of the manuscript.

Conflicts of interest

The authors do not have any conflict of interests to be declared.

Acknowledgements

This work was financially supported by “Région Occitanie” through a Readynov contract “Valorisation du CO₂ par méthanation catalytique» (2005314). Thanks to Marion Technologies for the scale-up of catalysts synthesized. TD and CHH are supported by the National Science Foundation through the Division of Materials Research under grant no. DMR-1956403 and the Camille and Henry Dreyfus Foundation. Computations were performed in the Extreme Science and Engineering Discovery Environment (XSEDE), which is supported by the National Science Foundation [ACI-1548562] and the PICS Coeus High Performance Computer, which is supported by the National Science Foundation [1624776]. The authors acknowledge Dr. Spiros Zafeiratos (ICPEES-UMR 7515 CNRS-ECPM-Strasbourg university, France) for access to XPS.

Notes and references

1. M. Thema, F. Bauer and M. Sterner, *Renewable and Sustainable Energy Reviews*, 2019, **112**, 775-787.
2. M. A. A. Aziz, A. A. Jalil, S. Triwahyono and A. Ahmad, *Green Chemistry*, 2015, **17**, 2647-2663.
3. L. Li, W. Zeng, M. Song, X. Wu, G. Li and C. Hu, *Catalysts*, 2022, **12**, 244.
4. Y. A. Daza and J. N. Kuhn, *RSC Advances*, 2016, **6**, 49675-49691.
5. M.-M. Millet, G. Algara-Siller, S. Wrabetz, A. Mazheika, F. Girgsdies, D. Teschner, F. Seitz, A. Tarasov, S. V. Levchenko, R. Schlögl and E. Frei, *Journal of the American Chemical Society*, 2019, **141**, 2451-2461.
6. H. Shen, Y. Dong, S. Yang, Y. He, Q. Wang, Y. Cao, W. Wang, T. Wang, Q. Zhang and H. Zhang, *Nano Research*, 2022, DOI: 10.1007/s12274-022-4207-8.
7. L. Wang, H. Liu, Y. Liu, Y. Chen and S. Yang, *Journal of Rare Earths*, 2013, **31**, 969-974.
8. C. Vogt, E. Groeneveld, G. Kamsma, M. Nachtegaal, L. Lu, C. J. Kiely, P. H. Berben, F. Meirer and B. M. Weckhuysen, *Nature Catalysis*, 2018, **1**, 127-134.
9. K. Feng, J. Tian, M. Guo, Y. Wang, S. Wang, Z. Wu, J. Zhang, L. He and B. Yan, *Applied Catalysis B: Environmental*, 2021, **292**, 120191.
10. L. R. Winter, E. Gomez, B. Yan, S. Yao and J. G. Chen, *Applied Catalysis B: Environmental*, 2018, **224**, 442-450.
11. H. C. Wu, Y. C. Chang, J. H. Wu, J. H. Lin, I. K. Lin and C. S. Chen, *Catalysis Science & Technology*, 2015, **5**, 4154-4163.
12. C. Rivera-Cárcamo, C. Scarfiello, A. B. García, Y. Tison, H. Martinez, W. Baaziz, O. Ersen, C. Le Berre and P. Serp, *Advanced Materials Interfaces*, 2021, **8**, 2001777.
13. B. Zhao, B. Yan, Z. Jiang, S. Yao, Z. Liu, Q. Wu, R. Ran, S. D. Senanayake, D. Weng and J. G. Chen, *Chemical Communications*, 2018, **54**, 7354-7357.
14. H. S. Lim, M. Lee, Y. Kim, D. Kang and J. W. Lee, *International Journal of Hydrogen Energy*, 2021, **46**, 15497-15506.
15. Y. Wang, L. R. Winter, J. G. Chen and B. Yan, *Green Chemistry*, 2021, **23**, 249-267.
16. B. Yan, B. Zhao, S. Kattel, Q. Wu, S. Yao, D. Su and J. G. Chen, *Journal of Catalysis*, 2019, **374**, 60-71.
17. N. Rui, X. Zhang, F. Zhang, Z. Liu, X. Cao, Z. Xie, R. Zou, S. D. Senanayake, Y. Yang, J. A. Rodriguez and C.-J. Liu, *Applied Catalysis B: Environmental*, 2021, **282**, 119581.
18. D. Messou, V. Bernardin, F. Meunier, M. B. Ordoño, A. Urakawa, B. F. Machado, V. Collière, R. Philippe, P. Serp and C. Le Berre, *Journal of Catalysis*, 2021, **398**, 14-28.
19. S. Tada, H. Nagase, N. Fujiwara and R. Kikuchi, *Energy & Fuels*, 2021, **35**, 5241-5251.
20. M.-X. Huang, F. Liu, C.-C. He, S.-Q. Yang, W.-Y. Chen, L. Ouyang and Y.-J. Zhao, *Chemical Physics Letters*, 2021, **768**, 138396.
21. G. Varvoutis, M. Lykaki, S. Stefa, V. Binas, G. E. Marnellos and M. Konsolakis, *Applied Catalysis B: Environmental*, 2021, **297**, 120401.
22. T. S. Galhardo, A. H. Braga, B. H. Arpini, J. Szanyi, R. V. Gonçalves, B. F. Zornio, C. R. Miranda and L. M. Rossi, *Journal of the American Chemical Society*, 2021, **143**, 4268-4280.
23. S. Lin, Q. Wang, M. Li, Z. Hao, Y. Pan, X. Han, X. Chang, S. Huang, Z. Li and X. Ma, *ACS Catalysis*, 2022, **12**, 3346-3356.
24. J. Guo, Z. Wang, J. Li and Z. Wang, *ACS Catalysis*, 2022, **12**, 4026-4036.
25. J. R. Rostrup-Nielsen and K. Pedersen, *Journal of Catalysis*, 1979, **59**, 395-404.
26. C. H. Bartholomew, G. D. Weatherbee and G. A. Jarvi, *Journal of Catalysis*, 1979, **60**, 257-269.

27. E. J. Erekson and C. H. Bartholomew, *Applied Catalysis*, 1983, **5**, 323-336.
28. C. H. Bartholomew, in *Studies in Surface Science and Catalysis*, eds. B. Delmon and G. F. Froment, Elsevier, 1987, vol. 34, pp. 81-104.
29. B. Legras, V. V. Ordonsky, C. Dujardin, M. Virginie and A. Y. Khodakov, *ACS Catalysis*, 2014, **4**, 2785-2791.
30. M. Wolf, C. Schüller and O. Hinrichsen, *Journal of CO₂ Utilization*, 2019, **32**, 80-91.
31. K. Müller, M. Fleige, F. Rachow and D. Schmeißer, *Energy Procedia*, 2013, **40**, 240-248.
32. X. Wen, L. Xu, M. Chen, Y. Shi, C. Lv, Y. Cui, X. Wu, G. Cheng, C.-e. Wu, Z. Miao, F. Wang and X. Hu, *Applied Catalysis B: Environmental*, 2021, **297**, 120486.
33. A. Alarcón, J. Guilera, R. Soto and T. Andreu, *Applied Catalysis B: Environmental*, 2020, **263**, 118346.
34. C. H. Rochester and R. J. Terrell, *Journal of the Chemical Society, Faraday Transactions 1: Physical Chemistry in Condensed Phases*, 1977, **73**, 609-621.
35. M. Trenary, K. J. Uram and J. T. Yates, *Surface Science*, 1985, **157**, 512-538.
36. W. Erley and H. Wagner, *Journal of Catalysis*, 1978, **53**, 287-294.
37. J. Heo, C. R. Staples and P. W. Ludden, *Biochemistry*, 2001, **40**, 7604-7611.
38. N. Y. Dzade and N. H. de Leeuw, *Catalysts*, 2021, **11**, 127.
39. M. M. Jaffar, M. A. Nahil and P. T. Williams, *Energy Technology*, 2019, **7**, 1900795.
40. M. Zhu, Q. Ge and X. Zhu, *Transactions of Tianjin University*, 2020, **26**, 172-187.
41. C.-T. Kuo, Y. Lu, L. Kovarik, M. Engelhard and A. M. Karim, *ACS Catalysis*, 2019, **9**, 11030-11041.
42. B. Wang, X. Li, S. Liang, R. Chu, D. Zhang, H. Chen, M. Wang, S. Zhou, W. Chen, X. Cao and W. Feng, *Physical Chemistry Chemical Physics*, 2020, **22**, 9943-9953.
43. W. Lin, H. Cheng, L. He, Y. Yu and F. Zhao, *Journal of Catalysis*, 2013, **303**, 110-116.
44. A. N. Mansour, *Surface Science Spectra*, 1994, **3**, 231-238.
45. A. N. Mansour and C. A. Melendres, *Surface Science Spectra*, 1994, **3**, 255-262.
46. J. Yu, Y. Hai and B. Cheng, *The Journal of Physical Chemistry C*, 2011, **115**, 4953-4958.
47. X. Zhang, Y. Chen, Y. Xiao, W. Zhou, G. Tian and H. Fu, *Nanoscale*, 2018, **10**, 4041-4050.
48. L. Hou, Q. Bu, S. Li, D. Wang and T. Xie, *RSC Advances*, 2016, **6**, 99081-99087.
49. J. Wang, Z. Yang, J. Mei, C. Wang, Q. Hong and S. Yang, *Journal of Colloid and Interface Science*, 2022, **622**, 431-442.
50. L. Zhang, I. S. Amiin, X. Ren, Z. Liu, G. Du, A. M. Asiri, B. Zheng and X. Sun, *Inorganic Chemistry*, 2017, **56**, 13651-13654.
51. H. Liu, Z. Liu, F. Wang and L. Feng, *Chemical Engineering Journal*, 2020, **397**, 125507.
52. T.-F. Hung, Z.-W. Yin, S. B. Betzler, W. Zheng, J. Yang and H. Zheng, *Chemical Engineering Journal*, 2019, **367**, 115-122.
53. Y. Nan, X. Wang, X. Ning, J. Lei, S. Guo, Y. Huang and J. Duan, *Surface and Coatings Technology*, 2019, **377**, 124935.
54. G. B. Shombe, M. D. Khan, C. Zequine, C. Zhao, R. K. Gupta and N. Revaprasadu, *Scientific Reports*, 2020, **10**, 3260.
55. A. Naldoni, M. Allieta, S. Santangelo, M. Marelli, F. Fabbri, S. Cappelli, C. L. Bianchi, R. Psaro and V. Dal Santo, *Journal of the American Chemical Society*, 2012, **134**, 7600-7603.
56. J. Strunk, W. C. Vining and A. T. Bell, *The Journal of Physical Chemistry C*, 2010, **114**, 16937-16945.
57. X. Pan, M.-Q. Yang, X. Fu, N. Zhang and Y.-J. Xu, *Nanoscale*, 2013, **5**, 3601-3614.
58. S.-H. Chien, Y.-W. Wei and M.-C. Lin, *Journal of the Chinese Chemical Society*, 1997, **44**, 195-201.
59. S. Mohajernia, P. Andryskova, G. Zoppellaro, S. Hejazi, S. Kment, R. Zboril, J. Schmidt and P. Schmuki, *Journal of Materials Chemistry A*, 2020, **8**, 1432-1442.
60. J. Li, Y. Lin, X. Pan, D. Miao, D. Ding, Y. Cui, J. Dong and X. Bao, *ACS Catalysis*, 2019, **9**, 6342-6348.
61. M. Xu, S. He, H. Chen, G. Cui, L. Zheng, B. Wang and M. Wei, *ACS Catalysis*, 2017, **7**, 7600-7609.
62. M. Xu, S. Yao, D. Rao, Y. Niu, N. Liu, M. Peng, P. Zhai, Y. Man, L. Zheng, B. Wang, B. Zhang, D. Ma and M. Wei, *Journal of the American Chemical Society*, 2018, **140**, 11241-11251.
63. Q. Pei, G. Qiu, Y. Yu, J. Wang, K. C. Tan, J. Guo, L. Liu, H. Cao, T. He and P. Chen, *The Journal of Physical Chemistry Letters*, 2021, **12**, 10646-10653.
64. A. Sarkar, D. Seth, M. Jiang, F. T. T. Ng and G. L. Rempel, *Topics in Catalysis*, 2014, **57**, 730-740.
65. M. Breyse, E. Furimsky, S. Kasztelan, M. Lacroix and G. Perot, *Catalysis Reviews*, 2002, **44**, 651-735.
66. C. H. Hendon, S. T. Hunt, M. Milina, K. T. Butler, A. Walsh and Y. Román-Leshkov, *The Journal of Physical Chemistry Letters*, 2016, **7**, 4475-4482.
67. D. Mondal, G. Villemure, G. Li, C. Song, J. Zhang, R. Hui, J. Chen and C. Fairbridge, *Applied Catalysis A: General*, 2013, **450**, 230-236.
68. G. Kresse and J. Furthmüller, *Physical Review B*, 1996, **54**, 11169-11186.
69. G. Kresse and J. Furthmüller, *Computational Materials Science*, 1996, **6**, 15-50.
70. J. P. Perdew, K. Burke and M. Ernzerhof, *Physical Review Letters*, 1996, **77**, 3865-3868.
71. P. E. Blöchl, *Physical Review B*, 1994, **50**, 17953-17979.
72. G. Kresse and D. Joubert, *Physical Review B*, 1999, **59**, 1758-1775.